Extended conformational states dominate the Hsp90 chaperone dynamics

Alexander Jussupow[1,‡] , Abraham Lopez[2,3,‡] , Mona Baumgart[2,‡], Sophie L. Mader[1] , Michael Sattler[2,3], and Ville R. I. Kaila[1,*]

From the [1]Department of Biochemistry and Biophysics, Stockholm University, Stockholm, Sweden; [2]Department Chemie, Center of Integrated Protein Science, Technische Universität München, Garching, Germany; [3]Institute of Structural Biology, Helmholtz Zentrum München, Neuherberg, Germany

Edited by Wolfgang Peti

The heat shock protein 90 (Hsp90) is a molecular chaperone central to client protein folding and maturation in eukaryotic cells. During its chaperone cycle, Hsp90 undergoes ATPase-coupled large-scale conformational changes between open and closed states, where the N-terminal and middle domains of the protein form a compact dimerized conformation. However, the molecular principles of the switching motion between the open and closed states remain poorly understood. Here we show by integrating atomistic and coarse-grained molecular simulations with small-angle X-ray scattering experiments and NMR spectroscopy data that Hsp90 exhibits rich conformational dynamics modulated by the charged linker, which connects the N-terminal with the middle domain of the protein. We show that the dissociation of these domains is crucial for the conformational flexibility of the open state, with the separation distance controlled by a β-sheet motif next to the linker region. Taken together, our results suggest that the conformational ensemble of Hsp90 comprises highly extended states, which could be functionally crucial for client processing.

The heat shock protein 90 (Hsp90) regulates protein folding in the eukaryotic cell (1–4). With over half of all human kinases being stringent clients of Hsp90, this ATP-dependent molecular chaperone is central for the regulation of the cell cycle, whereas its dysfunction is further implicated in the development of cancer (5, 6). Hsp90 consists of an ATP-binding N-terminal domain (NTD), a middle domain (MD), and a C-terminal domain (CTD), which are essential for dimerization of the protein (Fig. 1) (7). The Hsp90 dimer adopts an open conformation in the *apo* state, which recognizes misfolded proteins with its partially exposed hydrophobic regions (8–11). ATP binding and subsequent hydrolysis trigger conformational changes that lead to a closed, compact conformation where the NTDs and MDs dimerize (12–15). These domains are connected by a ∼60 aa long, primarily unstructured, and highly charged linker (CL) region, but its functional role in Hsp90 remains unclear (16–20). Notably,

residues close to the C-terminal end of the CL region (residues 265–269 for yeast Hsp90, β-strand 8) form a β-sheet with a β-strand of the NTD (residues 204–209, β-strand 7), which have been linked to Hsp90 activity and client binding (16, 20).

The conformational dynamics of Hsp90 has remained poorly understood, with a pronounced discrepancy between X-ray structures of Hsp90 and its homologs, and experimental studies of the Hsp90 dynamics in solution. In particular, the crystal structure of the nucleotide-bound closed state of Hsp90 has a radius of gyration (R_g) ∼41 Å (21–23) and a maximum dimension (D_{max}) ∼140 Å, whereas the resolved open conformations (24, 25) have an R_g ∼45 Å and D_{max} ∼150 Å. In contrast, small-angle X-ray scattering (SAXS) experiments (18, 19) indicate that the chaperone cycle could involve highly extended conformations with an average R_g >60 Å and D_{max} ∼250 Å (Fig. 1) that could be relevant for client protein recognition. These observations are further supported by optical tweezer experiments, where the extended conformations of Hsp90 are affected by the CL region (26). Moreover, the compact and partially open crystal structures differ in the orientation of NTD relative to the MD, indicative of possible dynamics between the domains (Fig. 1), which was demonstrated by a recent NMR study (11). However, the molecular details underlying this extended conformational dynamics still remain unresolved.

To probe the large-scale conformational dynamics of Hsp90, we apply here (∼20 µs) atomistic molecular dynamics (aMD) and (∼200 µs) coarse-grained molecular dynamics (cgMD) simulations (Table S1) in combination with SAXS and NMR spectroscopic experiments. We also perform mutagenesis experiments to investigate the effect of the CL region (Fig. S1).

Results

To explore the molecular details of the putative extended Hsp90 conformations, we first probed the dynamics of monomeric NTD-MD models of the yeast Hsp90. To this end, we combined extensive aMD simulations with experimental SAXS data (Figs. S2 and S3) using a Bayesian ensemble reweighting approach (Fig. 2A) (27). We performed the aMD simulations with the a99SB-disp force field (28), which

‡ These authors contributed equally to this work.
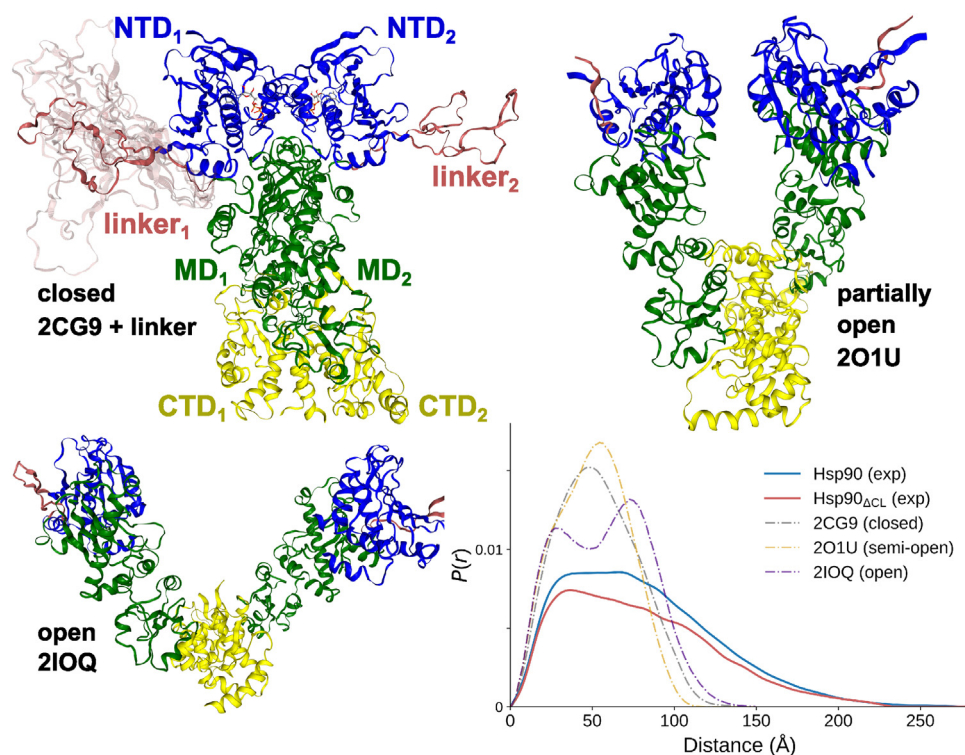* For correspondence: Ville R. I. Kaila, ville.kaila@dbb.su.se.

Figure 1. Overview of the Hsp90 dimer conformations. The closed X-ray structure of the Hsp90 dimer (PDB ID: 2CG9) with a modeled charged linker (CL) region (NTD in *blue*, CL in *red*, MD in *green*, CTD in *yellow*) (*top, left*). The rich linker dynamics obtained from aMD simulations is illustrated on the *left side* of the Hsp90 dimer. The partially open X-ray structure of GRP94 (PDB ID: 2O1U, *top right*), a homologous to Hsp90, and open dimer (PDB ID: 2IOQ, *bottom left*). The pair-distance distribution of the crystal structures is compared to profiles obtained from SAXS experiments (*bottom right*). Key features of the experimental $P(r)$ profile are not reproduced by the X-ray structures. CTD, C-terminal domain; MD, middle domain; NTD, N-terminal domain; PDB, Protein Data Bank.

accurately captures both folded and disordered protein states. For additional validation, we also conducted NMR experiments using a spin-label attached to an introduced Cys385 (13) of the MD to measure paramagnetic relaxation enhancements (PREs) effects on the NTD (Fig. S4). To investigate the effects of the CL dynamics, we deleted the linker region (residues 211–273) by site-directed mutagenesis experiments (NTD-MD$_{\Delta CL}$ construct) (see Experimental procedures, Figs. S1–S4). The SAXS-derived Guinier plots for the NTD-MD and NTD-MD$_{\Delta CL}$ constructs show no signs of aggregation (Fig. S3), indicating that both constructs are monodisperse, in contrast to a proposed NTD-driven dimerization model of the full-length Hsp90 (29).

Notably, in our atomistic molecular simulations of the NTD-MD construct, the NTD transiently separates from the MD, resulting in extended conformations and reproduces the experimental R_g of 36.5 Å (Figs. 2A and S5). The SAXS reweighted ensemble shows a unimodal R_g-distribution with a long tail for high R_g values. Based on the number of inter-domain contacts, we observe a 1:1 ratio between compact (average R_g of 34.1 Å) and extended conformations (average R_g of 38.8 Å), whereas a small fraction of highly extended conformations reaches an R_g of ∼57 Å (Fig. 2B) and are characterized by the partial unfolding of the β-sheet, formed by β-strand 7 of the NTD and β-strand 8 at the end of the CL, suggesting that the β-sheet limits the conformational flexibility

of the NTD/MD. As a result of this partial unfolding, the separation between the two domains can reach a distance of up to ∼66 Å, as compared to ∼27 Å for conformations with an intact NTD-CL β-sheet. The obtained structural ensemble accurately reproduces the extended tail of the experimental pair-distance distribution (Fig. 2C).

To validate these highly extended Hsp90 conformations, we next probed how the linker deletion affects the maximum extension of the protein. For the NTD-MD$_{\Delta CL}$ variant, where we both experimentally and computationally deleted the CL region (see Experimental procedures), we observe a substantial decrease in the experimental D_{max} (from ∼150 Å to ∼120 Å) and R_g (from 36.5 Å to 32.2 Å), as well as in the simulated D_{max} (from ∼163 Å to ∼151 Å) and the maximum R_g (from ∼57 Å to 39 Å) (Fig. S2 and Table S2). While the extension range between NTD and MD is highly reduced, the NTD-MD$_{\Delta CL}$ ensemble shows a 1:2 ratio between compact and extended conformations (Fig. 2A). Deletion of the linker region de-stabilizes the interaction between the NTD and MD by ∼1.6$k_B T$ (Fig. S6), an observation that is qualitatively consistent with optical tweezer experiments (26). The linker deletion thus limits the maximum extension of the protein (Fig. S6) and partially explains the lower D_{max} observed for the NTD-MD$_{\Delta CL}$ construct. In turn, the lack of β-sheet formation between NTD and CL around the β8 strand of the linker, disfavors interdomain interactions, thus rationalizing the
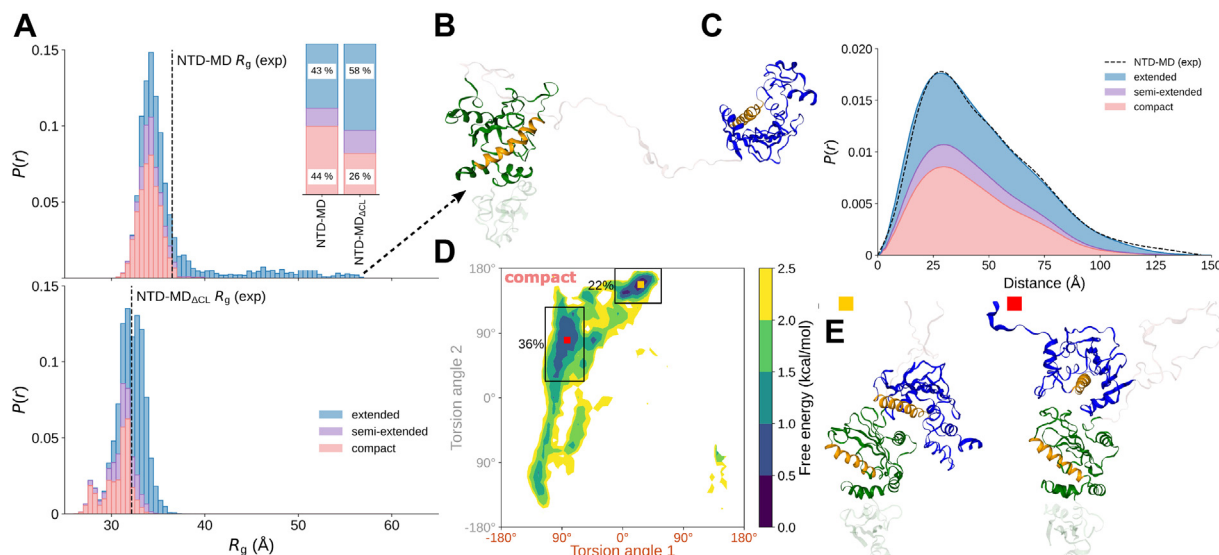
Figure 2. Conformational dynamics of the NTD-MD construct of Hsp90. *A*, distribution of the radius of gyration (R_g) obtained from SAXS reweighted aMD ensembles of the NTD-MD and NTD-MD$_{\Delta CL}$ constructs. The extended, partially open, and compact conformations are defined based on the number of residue contacts between the NTD (residue 20–202) and MD (residue 290–524) (0 for extended, >10 for the compact state). The intercept shows the ratio between compact, partially open, and extended states. *B*, structure of a highly extended conformation. *C*, pair-distance distribution of the reweighted NTD-MD ensemble. *D*, free energy profile of the compact state shown based on the torsion angles defined by the center of mass of residues 47 to 60, 178 to 188, 385 to 392, and 404 to 409 (torsion angle 1, in *orange*) and residues 64 to 69, 28 to 34, 395 to 403, and 367 to 370 (torsion angle 2, in *gray*). *E*, representative structures of highlighted regions in (*D*). aMD, atomistic molecular dynamics; MD, middle domain; NTD, N-terminal domain; SAXS, small-angle X-ray scattering.

relatively small differences in the average R_g between NTD-MD and NTD-MD$_{\Delta CL}$ construct.

Interdomain NMR-PRE measurements further support these large-scale conformational changes. Leu50, Leu56, and Leu62, located on the solvent-exposed end of the long helix α2 in the NTD (Fig. S7A), show distance-dependent PREs that are qualitatively consistent with an interdomain arrangement observed in the partially open state of GRP94, an endoplasmic reticulum chaperone that is homologous to Hsp90 (Protein Data Bank [PDB] ID: 2O1U) (24). In contrast, Val114, Ile117, and Val122, located at the NTD-MD interface, experience paramagnetic broadening expected for a closed conformation of yeast Hsp90 (Figs. 2B and S3). These structures differ by a ∼90° axial rotation of the NTD relative to MD, suggesting that additional extended conformations are involved in the transition between the two states observed in the PRE profile. Our aMD simulations qualitatively reproduce these features of the experimental PRE ratios (Fig. S4). The NTD-MD variant adopts a wide range of transient conformations, reflecting dynamics beyond the static crystal structures. The individual conformations show a wide distribution in the predicted interdomain residue distances due to the high flexibility observed in the aMD simulations (Figs. S7B, S8 and S9). Nevertheless, the majority of the compact conformations can be clustered in two distinct states (Fig. 2, *D* and *E*): about 22% of the compact structures show similarities to the partially open state, where the distances between Gln385 and the leucine cluster on helix α2 (Leu50/56/62) are considerably shorter than the distances to the NTD-MD interface (Val114/Ile117/Val122), corresponding to lower PRE ratios on helix α2. Moreover, in 36% of the compact conformations, the NTD-MD interface is closer to Gln385 and resembles the closed

state of Hsp90, with corresponding lower PRE ratios in this region (Fig. S6B). Overall, the energetic difference between these states is low, allowing for a rapid exchange between compact conformations (Fig. 2D). Additional conformational flexibility is observed for the ATP-lid segment (in the NTD), which samples open and closed conformations. Our combined data thus show that NTD-MD show a high level of flexibility, allowing the domains to dissociate and rotate relative to each other. These findings thus explain the extended distance distribution observed in our SAXS experiments.

We next probed how these large-scale conformational changes are reflected in the full-length Hsp90 dimer. To this end, we performed cgMD metadynamics simulations (see Experimental procedures) on the dimeric yeast Hsp90 with and without the linker region using the MARTINI3 force field (30), with modified protein–water interaction that better reproduces experimental data (31, 32). Moreover, we used AlphaFold2 (33) to assess the stability of secondary and tertiary structural elements (*via* the per-residue confidence score, pLDDT) and the relative flexibility between different regions and domains (*via* the predicted aligned error, PAE). Based on these scores, we constructed an elastic network for the cgMD simulations (Fig. S10). The obtained ensemble was further reweighted with SAXS data (Figs. 3 and S11) (27).

We obtain a low intradomain PAE for the NTD and MD-CTD, but large interdomain PAE between NTD and MD-CTD (Fig. S10A), indicating a high degree of positional and structural uncertainty. Unsurprisingly, the pLDDT score is low for the CL and the C-terminal end of Hsp90 (Fig. S10C), whereas the positional uncertainty between the CTDs is relatively small (Fig. S10B), as expected for their role in dimerization. The pLDDT and PAE scores also indicate that the β-sheet of the NTD-CL is stable.
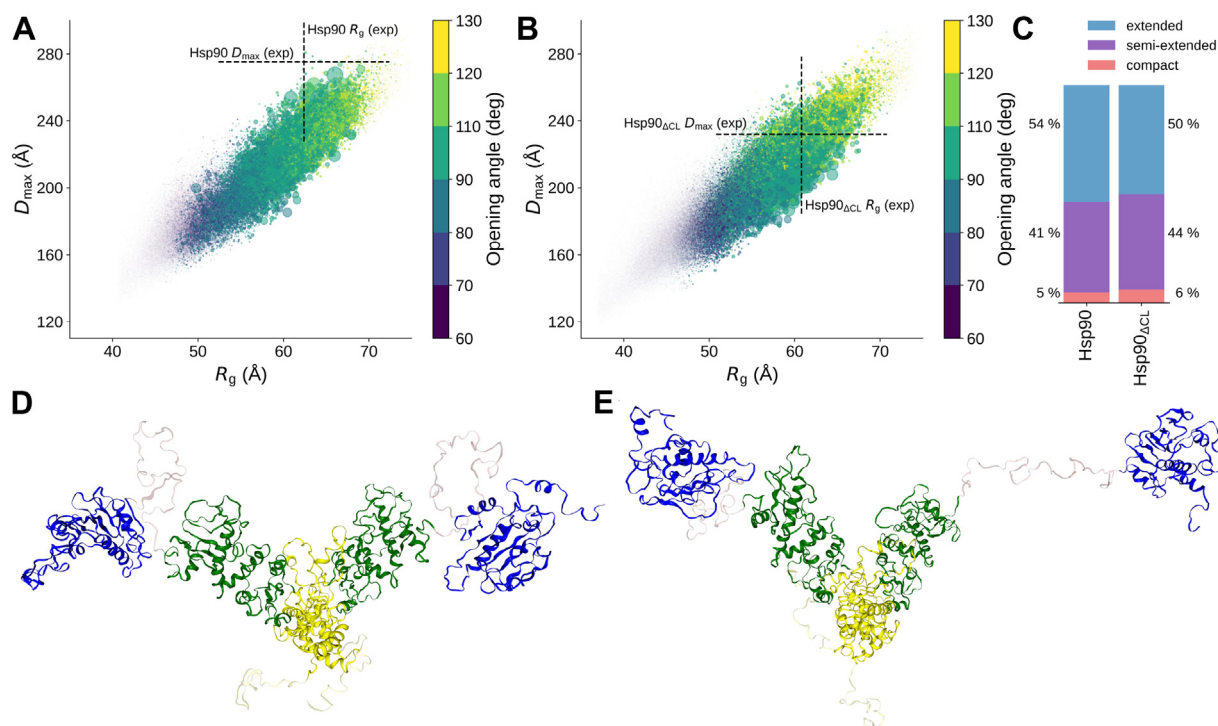
Figure 3. Dynamics of the full-length Hsp90. *A* and *B*, radius of gyration (R_g) as a function of maximum intermolecular distance (D_{max}) of the full-length. *A*, Hsp90 and (*B*) Hsp90$_{\Delta CL}$ ensemble. The size of the *circles* represents the weight of the individual conformations, while the color corresponds to the opening angle between MDs and the center of the CTDs. *C*, ratio between extended (no contacts between NTDs [residue 20–202] and MDs [residue 290–524]) and compact (contacts between NTDs and MDs of both chains) states. *D*, representative snapshot of the open "V-shape" conformation sampled during cgMD simulations. The representation shows the backbone beads and elastic network and bonds (NTD in *blue*, CL in *red*, MD in *green*, CTD in *yellow*). cgMD, coarse-grained molecular dynamics; CL, charged linker; CTD, C-terminal domain; MD, middle domain; NTD, N-terminal domain.

The cgMD simulations of Hsp90 and Hsp90$_{\Delta CL}$ suggest that the canonical closed and partially open conformations (Fig. 1) represent small parts of the overall ensemble of the *apo* state of Hsp90. Instead, we observe a dynamically highly flexible V-shaped state, with an average opening angle between MDs and CTD of ~102°, ranging between ~70° and ~130° in the simulations (Fig. 3), with a high correlation between the opening angle, R_g, and D_{max} values (Fig. 3, *A* and *B*). We observe predominantly extended conformations, with only around 5% of the ensembles in the compact state, in which both NTDs form direct contacts with the corresponding MD domains (Fig. 3*C*). The compact NTD-MD conformations are present in around ~28% and ~23% in the separate chains, with the individual NTD-MD modules dynamically rather independent of each other.

Upon removal of the CL region, our SAXS experiments show a significant reduction of the maximum dimension (from ~277 Å to ~233 Å), whereas the average R_g decreases by only 3% (from ~62 Å to ~60 Å). Similarly, as for the NTD-MD construct, the pair-distance distribution of the full-length Hsp90 shows a significant population at the extended distribution tail ($r > 230$ Å), which is not observed in the cut-linker construct, Hsp90$_{\Delta CL}$ (Fig. S11). We note that while our cgMD simulations reproduce the overall dynamics of the full-length Hsp90, inherent limitations of the elastic networks did not allow us to accurately sample the highly extended conformations with separated NTD-MD states as observed in the aMD

simulations of the NTD-MD constructs. However, by removing the elastic network that stabilizes the NTD-CL β-sheet, we observe highly extended states in the cgMD simulations, leading to a significant population at the extended pair-distance distribution tail (Fig. S12). This suggests that the Hsp90 dynamics could be highly sensitive to atomistic detail and protein–protein interactions.

Discussions

We have studied the conformational dynamics of Hsp90 using large-scale atomistic as well as coarse-grained molecular simulations and site-directed mutagenesis experiments combined with SAXS and NMR measurements. Our combined findings are summarized in Figure 4. We propose that open states of *apo* Hsp90 are in an equilibrium with a prevalent population of flexible extended states, defined by the separation of the NTD from the MD (Fig. 4, *panels 1* and *2*). This separation enables the relative rotation of the two domains (Fig. 4, *panel 3*). The highly CL region modulates the dissociation by the detachment of β-strand 8 of CL (residue 265–269) from β-strand 7 (residue 204–209) of NTD. A recent NMR study shows that this detachment leads to the exposure of a hydrophobic site mediating the binding of the p53 client protein to Hsp90 (20). These findings are in line with previous work showing the relevance of the β-strand 8 of the CL for the rotational flexibility of Hsp90, Aha1-mediated ATPase acceleration, and activation of specific clients (34).
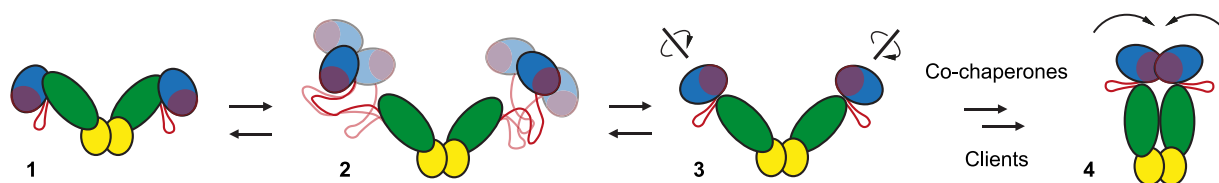
Figure 4. Role of the extended conformational landscape of Hsp90. In the absence of clients and cochaperones, Hsp90 exists in an equilibrium of open conformations involving detachment of the N-terminal domain (NTD) from the middle domain (MD, *panels 1* and *2*). These extended conformations allow the rotation and docking of the NTD with the MD upon nucleotide binding (*panel 3*), in a relative arrangement similar to that of the closed conformation of the dimer (*panel 4*). The binding of clients and cochaperones to specific regions of Hsp90 cause the shift toward the fully closed, active conformation of the dimer (*panel 4*).

As large surface regions are involved in the binding of cochaperones and client proteins (7), the extended Hsp90 conformations with different NTD-MD orientations could maximize the exposure of hydrophobic binding sites. The *apo* state of Hsp90 would thus avoid an ordered closed conformation until it is bound to a client, nucleotides, and/or cochaperones (Fig. 4, *panel 4*). Interestingly, similar behavior is also observed in other flexible multidomain proteins with a wide range of potential binding partners, such as in polyubiquitin chains (31). Although the exact biological significance of these extended conformations in Hsp90 remains unclear, we suggest that they are important in processing misfolded and unstructured clients that must be recognized in the crowded environment of the eukaryotic cell.

Experimental procedures

Molecular simulations

Atomistic Hsp90 models were built based on the crystal structure of yeast Hsp90 of the closed state (PDB ID: 2CG9) (21). The unresolved CL region was modeled using MODELLER (35). A monomeric Hsp90 model without the CTD was based on the closed state model and simulated for 2 × 2.25 μs in the *apo* state with and without the CL region (residues 211–273) using the a99SB-disp force field (28) with Gromacs (https://www.gromacs.org/) (36). Based on these simulations, we selected 24 starting conformations for additional 0.25 μs simulations, leading to a total of 10.5 μs simulations time for each construct (21 μs in total). The protein models were embedded in an extended water-ion environment with 100 mM NaCl allowing large-scale conformational changes. The complete simulation setups comprise *ca.* 542,000 atoms (NTD-MD construct) and 363,000 atoms (NTD-MD$_{\Delta CL}$ construct). The simulations were performed at T = 310 K, using a 2 fs timestep. A Bayesian/maximum entropy reweighting approach was used to reweight the a99SB-disp based molecular dynamics simulations with SAXS data (27). The PRE ratios from the ensembles were calculated using DEER-PREdict (https://github.com/KULL-Centre/DEERpredict) (37).

cgMD simulations with enhanced sampling of the dimeric full-length Hsp90 (with and without linker region) were created based on the atomistic models using the MARTINI3 coarse-grained force field (30). The cgMD models were embedded in a 100 mM NaCl solution in a 300 Å cubic box leading to *ca.* 165,000 beads. The simulations were performed at T = 310 K in an *NPT* ensemble with a 10 fs timestep using Gromacs (36) with PLUMED2 (38, 39). The protein–water interaction was increased by 6% to provide a better agreement with experimental data (31, 32). To conserve the secondary and tertiary protein structure, an elastic network model was introduced between residues with a high per-residue confidence score (pLDDT > 90) in AlphaFold2 (33). The strength of the network was determined based on the expected positional error calculated with AlphaFold2. The simulations were performed using parallel-biased metadynamics (40, 41) together with the multiple walker approach (42), including in total 48 replicas (for a total sampling time of 96 μs) using the distances and angles between the individual domains, as well as the radius of gyration, as collective variables. The metadynamics simulations were reweighted with SAXS data using a Bayesian/maximum entropy reweighting approach (27). An additional unbiased cgMD simulation was also performed without an elastic network stabilizing the NTD-CL β-sheet. A summary of all atomistic and coarse-grained simulations is shown in Tables S1 and S2.

Site-directed mutagenesis

The deletion of the CL residues 211 to 273 was introduced by site-directed mutagenesis using the QuikChange Lightning Mutagenesis Kit (Agilent), with primers ordered from Sigma–Aldrich, followed by PCR conducted according to the manufacturer's manual. The constructs were cloned using a pET28a-SUMO vector with an N-terminal His-SUMO-tag, and the plasmids were transformed into the *Escherichia coli* strain BL21 (DE3) cod+ (Stratagene).

Protein expression and purification of Hsp90 full-length and cut linker

The His-tagged yeast (*Saccharomyces cerevisiae*) Hsp90 with intact or cut CL was overexpressed in *E. coli* BL21 cells overnight at 30 °C after induction with 1 mM IPTG at A_{600} 0.8. The lysate was applied on a nickel–nitriloacetic acid affinity column after cell disruption, and the elution was digested with Tobacco Etch Virus overnight. The protein was purified using anion exchange chromatography, followed by size-exclusion chromatography (SEC) using a preparative Superdex 200pg HiLoad 16/600 column (GE Healthcare).

Protein expression and purification of NTD-MD construct

The fusion protein was overexpressed in *E. coli* BL21 Rosetta cells. The cells were grown at 37 °C until an A_{600} 0.8 was reached. After induction with 1 mM IPTG the expression took place during 2 days at 18 °C. The constructs were purified using nickel–nitriloacetic acid after cell lysis, and the SUMO cleavage was conducted overnight. The protein was purified using anion exchange chromatography, followed by SEC using a preparative Superdex 75pg HiLoad 16/600 column (GE Healthcare).

SAXS measurements

SAXS data were collected at the BM29 beamline at the European Synchrotron Radiation Facility for yeast Hsp90 and at the Swing beamline at the Soleil synchrotron for the rest of the samples. Forty to fifty microliters sample in 25 mM Hepes pH 7.5, 150 mM KCl, 5 mM $MgCl_2$, 1 mM Tris(2-carboxyethyl)phosphine, and 0.02% NaN_3 was injected to a Superdex 200 5/150 GL column (GE Healthcare) connected online to the SAXS capillary. One SAXS frame per second was recorded at a flow rate of 0.15 ml min^{-1}. SEC-SAXS chromatograms were analyzed using the Chromixs software (https://www.embl-hamburg.de/biosaxs/chromixs.html) (43), for which buffer frames with constant average intensity were selected from the chromatogram. The subtracted averaged scattering profiles were analyzed using the Primus package using RAW 1.6.3 (44) to extract R_g values and $P(r)$ distributions.

PRE experiments

The NTD-MD construct with the Q385C mutation was produced following the same protocol as for the WT protein but using 99.9% D_2O in a M9 medium for cell growth. ILVM labeling was conducted by adding 250 mg methyl-^{13}C Met, 50 mg 2-ketobutyric 4-^{13}C 3, 3-D_2, and 100 mg 2-keto-(3-methyl-^{13}C)-butyric 4-^{13}C 3-D 1 h prior induction (amounts for 1 l). Purification was performed analogously but including 2 mM DTT in all buffers. After the size exclusion step, the protein was exchanged to 1 M Tris–HCl pH 8, 200 mM NaCl, and ten equivalents of 3-(2-iodacetamido)-PROXYL was added followed by incubation in the dark at 4 °C overnight. Afterward, the sample was exchanged to 20 mM Tris D_{11}-HCl pH 7, 100 mM NaCl, 5 mM $MgCl_2$, 2 mM DTT-D_{10}, in 99.9% D_2O. A ^{1}H-^{13}C methyl-transverse relaxation optimized spectroscopy spectrum of the oxidized form was recorded at 303 K in a 22.31 T (950 MHz ^{1}H) magnetic field spectrometer, using a 3 s interscan delay. Chemical shift assignments were obtained from previous work (45). Theoretical intensity ratios were extracted from PDB coordinates or simulated structures using the method described by Simon *et al.* (46) and Lapinaite *et al.* (47).

Data availability

The data that support the findings of this study are available on request from the corresponding author V. R. I. K. The simulation trajectories can be found in Zenodo, https://doi.org/10.5281/zenodo.6685254.

References

1. Nathan, D. F., Vos, M. H., and Lindquist, S. (1997) *In vivo* functions of the Saccharomyces cerevisiae Hsp90 chaperone. *Proc. Natl. Acad. Sci. U. S. A.* **94**, 12949–12956
2. Picard, D. (2002) Heat-shock protein 90, a chaperone for folding and regulation. *Cell. Mol. Life Sci.* **59**, 1640–1648
3. Young, J. C., Agashe, V. R., Siegers, K., and Hartl, F. U. (2004) Pathways of chaperone-mediated protein folding in the cytosol. *Nat. Rev. Mol. Cell Biol.* **5**, 781–791
4. Taipale, M., Jarosz, D. F., and Lindquist, S. (2010) HSP90 at the hub of protein homeostasis: emerging mechanistic insights. *Nat. Rev. Mol. Cell Biol.* **11**, 515–528

5. Isaacs, J. S., Xu, W., and Neckers, L. (2003) Heat shock protein 90 as a molecular target for cancer therapeutics. *Cancer Cell* **3**, 213–217

6. Taipale, M., Krykbaeva, I., Koeva, M., Kayatekin, C., Westover, K. D., Karras, G. I., *et al.* (2012) Quantitative analysis of HSP90-client interactions reveals principles of substrate recognition. *Cell* **150**, 987–1001

7. Schopf, F. H., Biebl, M. M., and Buchner, J. (2017) The HSP90 chaperone machinery. *Nat. Rev. Mol. Cell Biol.* **18**, 345–360

8. Krukenberg, K. A., Street, T. O., Lavery, L. A., and Agard, D. A. (2011) Conformational dynamics of the molecular chaperone Hsp90. *Q. Rev. Biophys.* **44**, 229–255

9. Kim, Y. E., Hipp, M. S., Bracher, A., Hayer-Hartl, M., and Hartl, F. U. (2013) Molecular chaperone functions in protein folding and proteostasis. *Annu. Rev. Biochem.* **82**, 323–355

10. Oroz, J., Kim, J. H., Chang, B. J., and Zweckstetter, M. (2017) Mechanistic basis for the recognition of a misfolded protein by the molecular chaperone Hsp90. *Nat. Struct. Mol. Biol.* **24**, 407–413

11. Lopez, A., Dahiya, V., Delhommel, F., Freiburger, L., Stehle, R., Asami, S., *et al.* (2021) Client binding shifts the populations of dynamic Hsp90 conformations through an allosteric network. *Sci. Adv.* **7**, eabl7295

12. Wegele, H., Muschler, P., Bunck, M., Reinstein, J., and Buchner, J. (2003) Dissection of the contribution of individual domains to the ATPase mechanism of Hsp90. *J. Biol. Chem.* **278**, 39303–39310

13. Hessling, M., Richter, K., and Buchner, J. (2009) Dissection of the ATP-induced conformational cycle of the molecular chaperone Hsp90. *Nat. Struct. Mol. Biol.* **16**, 287–293

14. Mickler, M., Hessling, M., Ratzke, C., Buchner, J., and Hugel, T. (2009) The large conformational changes of Hsp90 are only weakly coupled to ATP hydrolysis. *Nat. Struct. Mol. Biol.* **16**, 281–286

15. Hellenkamp, B., Wortmann, P., Kandzia, F., Zacharias, M., and Hugel, T. (2017) Multidomain structure and correlated dynamics determined by self-consistent FRET networks. *Nat. Methods* **14**, 174–180

16. Tsutsumi, S., Mollapour, M., Graf, C., Lee, C. T., Scroggins, B. T., Xu, W., *et al.* (2009) Hsp90 charged-linker truncation reverses the functional consequences of weakened hydrophobic contacts in the N domain. *Nat. Struct. Mol. Biol.* **16**, 1141–1147

17. Tsutsumi, S., Mollapour, M., Prodromou, C., Lee, C. T., Panaretou, B., Yoshida, S., *et al.* (2012) Charged linker sequence modulates eukaryotic heat shock protein 90 (Hsp90) chaperone activity. *Proc. Natl. Acad. Sci. U. S. A.* **109**, 2937–2942

18. Lorenz, O. R., Freiburger, L., Rutz, D. A., Krause, M., Zierer, B. K., Alvira, S., *et al.* (2014) Modulation of the Hsp90 chaperone cycle by a stringent client protein. *Mol. Cell* **53**, 941–953

19. Mader, S. L., Lopez, A., Lawatscheck, J., Luo, Q., Rutz, D. A., Gamiz-Hernandez, A. P., *et al.* (2020) Conformational dynamics modulate the catalytic activity of the molecular chaperone Hsp90. *Nat. Commun.* **11**, 1410

20. López, A., Elimelech, A. R., Klimm, K., and Sattler, M. (2021) The charged linker modulates the conformations and molecular interactions of Hsp90. *ChemBioChem* **22**, 1084–1092

21. Ali, M. M., Roe, S. M., Vaughan, C. K., Meyer, P., Panaretou, B., Piper, P. W., *et al.* (2006) Crystal structure of an Hsp90-nucleotide-p23/Sba1 closed chaperone complex. *Nature* **440**, 1013–1017

22. Lavery, L. A., Partridge, J. R., Ramelot, T. A., Elnatan, D., Kennedy, M. A., and Agard, D. A. (2014) Structural asymmetry in the closed state of mitochondrial Hsp90 (TRAP1) supports a two-step ATP hydrolysis mechanism. *Mol. Cell* **53**, 330–343

23. Huck, J. D., Que, N. L., Hong, F., Li, Z., and Gewirth, D. T. (2017) Structural and functional analysis of GRP94 in the closed state reveals an essential role for the pre-N domain and a potential client-binding site. *Cell Rep.* **20**, 2800–2809

24. Dollins, D. E., Warren, J. J., Immormino, R. M., and Gewirth, D. T. (2007) Structures of GRP94-nucleotide complexes reveal mechanistic differences between the hsp90 chaperones. *Mol. Cell* **28**, 41–56

25. Shiau, A. K., Harris, S. F., Southworth, D. R., and Agard, D. A. (2006) Structural analysis of E. coli hsp90 reveals dramatic nucleotide-dependent conformational rearrangements. *Cell* **127**, 329–340

26. Jahn, M., Rehn, A., Pelz, B., Hellenkamp, B., Richter, K., Rief, M., *et al.* (2014) The charged linker of the molecular chaperone Hsp90 modulates domain contacts and biological function. *Proc. Natl. Acad. Sci. U. S. A.* **111**, 17881–17886

27. Bottaro, S., Bengtsen, T., and Lindorff-Larsen, K. (2020) Integrating molecular simulation and experimental data: a Bayesian/maximum entropy reweighting approach. *Methods Mol. Biol.* **2112**, 219–240

28. Robustelli, P., Piana, S., and Shaw, D. E. (2018) Developing a molecular dynamics force field for both folded and disordered protein states. *Proc. Natl. Acad. Sci. U. S. A.* **115**, E4758–E4766

29. Ratzke, C., Mickler, M., Hellenkamp, B., Buchner, J., and Hugel, T. (2010) Dynamics of heat shock protein 90 C-terminal dimerization is an important part of its conformational cycle. *Proc. Natl. Acad. Sci. U. S. A.* **107**, 16101–16106

30. Souza, P. C. T., Alessandri, R., Barnoud, J., Thallmair, S., Faustino, I., Grunewald, F., *et al.* (2021) Martini 3: a general purpose force field for coarse-grained molecular dynamics. *Nat. Methods* **18**, 382–388

31. Jussupow, A., Messias Ana, C., Stehle, R., Geerlof, A., Solbak Sara, M.Ø., Paissoni, C., *et al.* (2020) The dynamics of linear polyubiquitin. *Sci. Adv.* **6**, eabc3786

32. Thomasen, F. E., Pesce, F., Roesgaard, M. A., Tesei, G., and Lindorff-Larsen, K. (2022) Improving Martini 3 for disordered and multidomain proteins. *J. Chem. Theory Comput.* **18**, 2033–2041

33. Jumper, J., Evans, R., Pritzel, A., Green, T., Figurnov, M., Ronneberger, O., *et al.* (2021) Highly accurate protein structure prediction with AlphaFold. *Nature* **596**, 583–589

34. Daturpalli, S., Kniess, R. A., Lee, C. T., and Mayer, M. P. (2017) Large rotation of the N-terminal domain of Hsp90 is important for interaction with some but not all client proteins. *J. Mol. Biol.* **429**, 1406–1423

35. Sali, A., and Blundell, T. L. (1993) Comparative protein modelling by satisfaction of spatial restraints. *J. Mol. Biol.* **234**, 779–815

36. Abraham, M. J., Murtola, T., Schulz, R., Páll, S., Smith, J. C., Hess, B., *et al.* (2015) GROMACS: high performance molecular simulations through multi-level parallelism from laptops to supercomputers. *SoftwareX* **1-2**, 19–25

37. Tesei, G., Martins, J. M., Kunze, M. B. A., Wang, Y., Crehuet, R., and Lindorff-Larsen, K. (2021) DEER-PREdict: software for efficient calculation of spin-labeling EPR and NMR data from conformational ensembles. *PLoS Comput. Biol.* **17**, e1008551

38. Tribello, G. A., Bonomi, M., Branduardi, D., Camilloni, C., and Bussi, G. (2014) PLUMED 2: new feathers for an old bird. *Comput. Phys. Commun.* **185**, 604–613

39. consortium, P. (2019) Promoting transparency and reproducibility in enhanced molecular simulations. *Nat. Methods* **16**, 670–673

40. Pfaendtner, J., and Bonomi, M. (2015) Efficient sampling of high-dimensional free-energy landscapes with parallel bias metadynamics. *J. Chem. Theory Comput.* **11**, 5062–5067

41. Laio, A., and Parrinello, M. (2002) Escaping free-energy minima. *Proc. Natl. Acad. Sci. U. S. A.* **99**, 12562–12566

42. Raiteri, P., Laio, A., Gervasio, F. L., Micheletti, C., and Parrinello, M. (2006) Efficient reconstruction of complex free energy landscapes by multiple walkers metadynamics. *J. Phys. Chem. B* **110**, 3533–3539

43. Panjkovich, A., and Svergun, D. I. (2018) CHROMIXS: automatic and interactive analysis of chromatography-coupled small-angle X-ray scattering data. *Bioinformatics* **34**, 1944–1946

44. Hopkins, J. B., Gillilan, R. E., and Skou, S. (2017) BioXTAS RAW: improvements to a free open-source program for small-angle X-ray scattering data reduction and analysis. *J. Appl. Crystallogr.* **50**, 1545–1553

45. Biebl, M. M., Lopez, A., Rehn, A., Freiburger, L., Lawatscheck, J., Blank, B., *et al.* (2021) Structural elements in the flexible tail of the co-chaperone p23 coordinate client binding and progression of the Hsp90 chaperone cycle. *Nat. Commun.* **12**, 828

46. Simon, B., Madl, T., Mackereth, C. D., Nilges, M., and Sattler, M. (2010) An efficient protocol for NMR-spectroscopy-based structure determination of protein complexes in solution. *Angew. Chem. Int. Ed. Engl.* **49**, 1967–1970

47. Lapinaite, A., Simon, B., Skjaerven, L., Rakwalska-Bange, M., Gabel, F., and Carlomagno, T. (2013) The structure of the box C/D enzyme reveals regulation of RNA methylation. *Nature* **502**, 519–523